Cation-induced monolayer collapse at lower surface pressure follows specific headgroup percolation

Kaushik Das, Bijay Kumar Sah, and Sarathi Kundu*

Soft Nano Laboratory, Physical Sciences Division, Institute of Advanced Study in Science and Technology, Vigyan Path, Paschim Boragaon, Garchuk, Guwahati, Assam 781035, India

(Received 11 November 2016; revised manuscript received 6 January 2017; published 13 February 2017)

A Langmuir monolayer can be considered as a two-dimensional (2D) sheet at higher surface pressure which structurally deform with mechanical compression depending upon the elastic nature of the monolayer. The deformed structures formed after a certain elastic limit are called collapsed structures. To explore monolayer collapses at lower surface pressure and to see the effect of ions on such monolayer collapses, out-of-plane structures and in-plane morphologies of stearic acid Langmuir monolayers have been studied both at lower (≈6.8) and higher (≈9.5) subphase *p*H in the presence of Mg^{2+}, Ca^{2+}, Zn^{2+}, Cd^{2+}, and Ba^{2+} ions. At lower subphase *p*H and in the presence of all cations, the stearic acid monolayer remains as a monolayer before collapse, which generally takes place at higher surface pressure ($\pi_c > 50$ mN/m). However, at higher subphase *p*H, structural changes of stearic acid monolayers occur at relatively lower surface pressure depending upon the specific dissolved ions. Among the same group elements of Mg^{2+}, Ca^{2+}, and Ba^{2+}, only for Ba^{2+} ions does monolayer to multilayer transition take place from a much lower surface pressure of the monolayer, remaining, however, as a monolayer for Mg^{2+} and Ca^{2+} ions. For another same group elements of Zn^{2+} and Cd^{2+} ions, a less covered bilayer structure forms on top of the monolayer structure at lower surface pressure, which is evidenced from both x-ray reflectometry and atomic force microscopy. Fourier transform infrared spectroscopy confirms the presence of two coexisting conformations formed by the two different metal-headgroup coordinations and the monolayer to trilayer or multilayer transformation takes place when the coverage ratio of the two molecular conformations changes from the critical value (p_c) of ≈ 0.66. Such ion-specific monolayer collapses are correlated with the 2D lattice percolation model.

DOI: 10.1103/PhysRevE.95.022804

I. INTRODUCTION

Langmuir monolayers have been extensively studied throughout the last few decades to explore their structures, phases, phase transitions, probable applications, etc. [1–3]. Langmuir monolayers of fatty acids and lipids at the air-water interface are treated as model systems [3] to study different phenomena related to thermodynamics [3], molecular recognitions [4–6], membrane behaviors [7–9], etc. Langmuir monolayers can be considered as two-dimensional (2D) sheets at higher surface pressure [10–12] where a condensed phase is formed and the structural deformation of such sheets with mechanical compression is related with the elastic nature of the monolayers; however, the mechanisms of forming such structural deformations are not fully understood yet. The compression of Langmuir monolayers by means of mechanical barriers leads to phase transitions through several 2D phases such as gaseous, liquid expanded, liquid condensed, condensed, etc. [1–3]. These phases can be inferred from the different slopes of the surface pressure vs specific molecular area (π-A) isotherms [2,13], Brewster angle microscopy [14], grazing incidence x-ray diffraction (GIXRD) [2,3], polarized modulation infrared reflection absorption spectroscopy [15], etc. Further compression beyond the condensed phase leads to the monolayer collapse and hence 2D to 3D structural transformation takes place [16–19]. In general, monolayer collapse occurs at higher surface pressure called collapse pressure (π_c) ($\pi_c \geqslant 50$ mN/m) through two different ways [1,2,20–22]: "constant area collapse" where surface pressure suddenly drops just after π_c and "constant pressure collapse" where surface pressure remains nearly constant after π_c [16,17]. According to the "Ries model," monolayer collapse occurs through four steps, viz., weakening, folding, bending, and breaking [16]. Birdi and Vu showed the presence of monolayer, bilayer, and trilayer structures in collapsed stearic acid films through atomic force microscopy (AFM) [18]. Moreover, monolayers folding into subphase, buckling, 3D grain, or islands formation, etc., are proposed by different groups [23,24]. Phase contrast microscopy of stearic acid monolayer reveals the crack pattern leading to collapse [25,26]. However, below π_c, monolayer to multilayer domain formation has also been observed with time at constant surface pressure through lipophilic interaction [27]. Generally, monolayer collapses are an irreversible process, however, reversible monolayer collapse is also observed for certain mixed monolayers like those of lung surfactants where the surface tension regulates lung functional operation [24,28,29]. Biological processes such as fission and fusion of cell membranes are related with the collapse processes [30–32].

Structural transformation of monolayers depends upon several physicochemical parameters such as temperature, pressure, molecular concentration, compression speed, dissolved ions, subphase *p*H, added molecules, etc. [1–3,33–42]. Moreover, monolayer collapses highly depend on dissolved ions and subphase *p*H [20–22,43,44]. In the presence of cadmium ions at higher subphase *p*H and lower temperature, the arachidic acid monolayer collapses through buckling [45]. A transition from constant area collapse to constant pressure collapse has also been observed for a stearic acid Langmuir monolayer from phase contrast microscopy and π-A isotherms [25,26] with the variation of subphase *p*H

*Corresponding author: sarathi.kundu@gmail.com

and dissolved ions. Interactions between cation-cation and cation-headgroup are the key reasons behind such different collapse behaviors. In-plane and out-of-plane structures before and after monolayer collapses have already been studied through GIXRD, x-ray reflectivity (XRR), and AFM on both air-water and air-solid interfaces [19,23,46–51]. Monolayer collapses at higher surface pressure ($\pi_c \geqslant 50$ mN/m) have been studied, but reports on lower pressure collapse, i.e., far below the conventional π_c value, are much fewer. It has been reported that a 1,2-dipalmitoyl-sn-glycero-3-phosphocholine (DPPC) Langmuir monolayer in the presence of butylparabens collapses at lower surface pressure [52]. At high subphase pH, monolayer to multilayer collapse of a stearic acid monolayer in the presence of barium ions has also been reported [53]. Fourier transform infrared (FTIR) data show that the formation of bidentate chelate coordination is the key reason behind such monolayer to multilayer transformation [53]. It has already been revealed from FTIR spectroscopy that the metal-headgroup coordination in Langmuir monolayers occurs in three different ways: unidentate, bidentate bridging, and bidentate chelate coordinations [54]. At lower subphase pH, the metal-headgroup coordination is unidentate and with the pH increment the headgroup coordination modifies to bidentate bridging, bidentate chelate, or both [55,56]. Although morphological and structural modifications, growth, and mechanisms of monolayer collapses are explored, a deeper understanding on monolayer collapses depending upon subphase physicochemical conditions is still incomplete. Recently, the collapse of mixed lipid monolayers has been explained using the concept of the lattice percolation phenomenon [49,57]. As fatty acid molecules form a 2D lattice at the air-water interface with different bonding configurations in the headgroups, the principles of a 2D lattice percolation model [58–60] can also be applied in explaining the monolayer collapses. Generally, percolation theory deals with the systems for which connected pathways exist in lattices whose bonds or sites are occupied to different extents. The percolation threshold for a 2D lattice is the fraction of occupied bonds or sites that are connected through nearest neighbors over the entire lattice. In rigidity percolation this concept is further extended to vectorial long-range connectivities to form a connected lattice that will be rigid with respect to applied forces [58–60]. Concepts of percolation theory are applicable in different areas of research including communications, biology, physics, geophysics, engineering, etc.

In this article we have shown the structural modifications of a stearic acid monolayer in the presence of different divalent ions, e.g., Mg^{2+}, Ca^{2+}, Zn^{2+}, Cd^{2+}, and Ba^{2+} ions, as the elastic nature of the monolayer modifies in the presence of different cations. Out-of-plane structures and the surface morphologies are obtained from the XRR and AFM studies after depositing the films on hydrophilic Si (001) substrates by using the Langmuir-Blodgett (LB) method. At lower subphase pH (≈6.8) and lower surface pressure ($\pi = 25$ mN/m), metal-stearate (M-St, M = Mg, Ca, Zn, Cd, Ba) molecules form a monolayer on the water surface and are deposited as a monolayer on the Si (001) substrates. At higher subphase pH (≈9.5), multilayer structures of BaSt form on the water surface and are deposited as a multilayer in a single up stroke of the hydrophilic Si (001) substrate at 25 mN/m. However, for CdSt and ZnSt, trilayer structures have been deposited at $\pi = 25$ mN/m in a single up stroke. CaSt and MgSt remain as monolayers on the water surface at higher subphase pH (≈9.5) and are deposited as monolayers on Si (001) substrates in a single up stroke at the same deposition pressure ($\pi = 25$ mN/m). The elastic nature of the monolayer which is microscopically decided by the formation of specific metal-headgroup coordination plays a crucial role in the structural transformation of the monolayers at high subphase pH which is obtained from FTIR spectroscopy. Two-dimensional percolated networks formed by the two different forms of the metal-headgroup coordinations are responsible for such different monolayer collapses.

II. EXPERIMENTAL DETAILS

Stearic acid [$CH_3(CH_2)_{16}COOH$, Sigma, 99%] molecules were spread from a 0.5 mg/ml chloroform (Aldrich, 99%) solution on Milli-Q water (resistivity 18.2 MΩ cm) containing barium chloride ($BaCl_2 \cdot 2H_2O$, Merck, 99%), magnesium chloride ($MgCl_2 \cdot 6H_2O$, Merck, 99%), cadmium chloride ($CdCl_2 \cdot H_2O$, Merck, 99%), zinc chloride ($ZnCl_2$, Merck, 99%), or calcium chloride ($CaCl_2 \cdot 2H_2O$, Merck, 99%) in a Langmuir trough (Apex Instruments). All salt concentrations were of ≈0.5 mM and pH of the water subphase was maintained at ≈6.8 and 9.5 for each salt. No buffer was used to maintain the pH of the subphase. π was measured with a paper Wilhelmy plate and the monolayer was compressed at a constant rate of 5 mm/min during all isotherm measurements and film depositions. All depositions were done by using the LB method in a single up stroke at 25 mN/m and at room temperature (24 °C). Depositions were carried out at a speed of 1.5 mm/min. Prior to the deposition, Si(001) substrates were made hydrophilic by keeping them in a mixed solution of ammonium hydroxide (NH_4OH, Merck, 30%), hydrogen peroxide (H_2O_2, Merck, 30%), and Milli-Q water ($H_2O : NH_4OH : H_2O_2 = 2 : 1 : 1$, by volume) for 5–10 min at 100 °C. Immediately after cleaning, all the substrates were kept inside the Milli-Q water until LB deposition.

XRR measurements were carried out using a versatile x-ray diffractometer setup. The diffractometer (D8 Advanced, Bruker AXS) consists of a Cu source (sealed tube) followed by a Göbel mirror to select and enhance Cu $K\alpha$ radiation ($\lambda = 1.54$ Å). A scattered beam was detected using a NaI scintillation (point) detector. The data were taken in specular condition, i.e., the incident angle (θ) is equal to the reflected angle (θ) and both are in a scattering plane. Under such condition, a nonvanishing wave-vector component, q_z, exists which is given by $(4\pi/\lambda)\sin\theta$. The XRR technique essentially provides an electron density profile (EDP), i.e., in-plane ($x - y$) average electron density (ρ) as a function of depth (z) in high resolution [61,62]. From EDP it is possible to estimate film thickness, electron density, and interfacial roughness [61,63]. An analysis of XRR data has been carried out using Parratt's formalism where the film is considered as a stack of multiple homogeneous layers [64]. The surface topography of all the deposited films was studied through AFM (NTEGRA Prima, NT-MDT Technology) in semicontact mode using a silicon cantilever having a spring constant of ≈11.8 N/m. Scans were performed over several portions of the films for

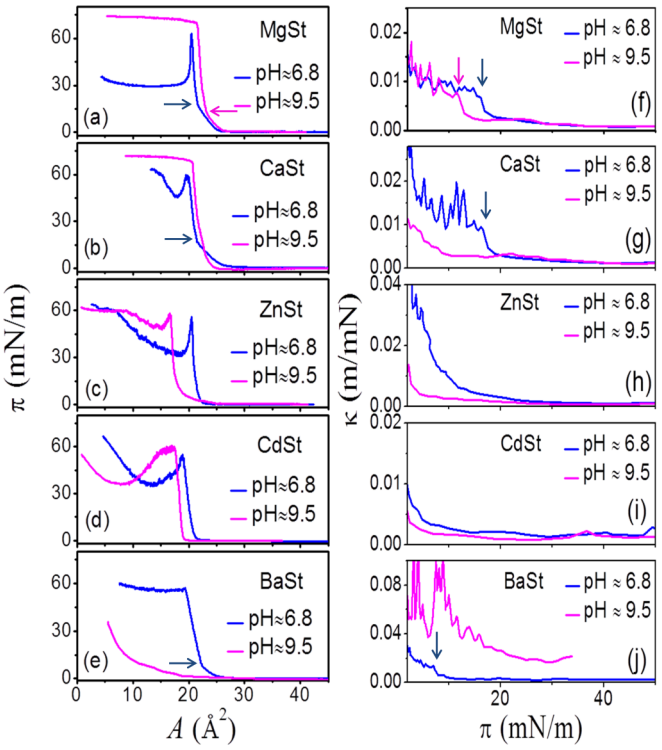

FIG. 1. Left column: Surface pressure (π); specific molecular area (A); isotherms of stearic acid Langmuir monolayers in the presence of (a) Mg^{2+}, (b) Ca^{2+}, (c) Zn^{2+}, (d) Cd^{2+}, and (e) Ba^{2+} ions at lower (≈6.8) (blue lines) and higher (≈9.5) (magenta lines) subphase pH. Right column: Variation of isothermal compressibility (κ) with the monolayer surface pressure (π) in the presence of (f) Mg^{2+}, (g) Ca^{2+}, (h) Zn^{2+}, (i) Cd^{2+}, and (j) Ba^{2+} ions in subphase water and for two different subphase pH. Arrows indicate the phase transition points.

different scan areas. WSXM software [65] is used for AFM image processing and analysis. The attenuated total reflection–Fourier transform infrared (ATR-FTIR) spectroscopy data were taken using a NICOLET 6700 (Thermo-Fisher) spectrophotometer in the wave number range of 380 – 4000 cm^{-1} at 4 cm^{-1} resolution.

III. RESULTS AND DISCUSSION

π-A isotherms for stearic acid Langmuir monolayers in the presence of Ca^{2+}, Mg^{2+}, Cd^{2+}, Zn^{2+}, and Ba^{2+} ions in aqueous subphase have been shown in Figs. 1(a)–1(e), respectively, for both lower (≈6.8) and higher (≈9.5) subphase pH. At lower subphase pH and in the presence of both Mg^{2+} and Ca^{2+} ions, the tilted to untilted phase transition point in the stearic acid monolayer is indicated by an arrow which occurs at ≈17 mN/m as shown in Figs. 1(a) and 1(b), respectively; however, monolayer collapse occurs at $\pi_c \approx 63$ and 59 mN/m for Mg^{2+} and Ca^{2+} ions, and the corresponding area per molecule at collapse point, i.e., A_c, is ≈ 20.5 and 19.8 $Å^2$, respectively. However, for higher subphase pH conditions, the magnesium stearate (MgSt) monolayer shows a tilted to untilted phase transition at ≈13.5 mN/m, which is indicated by an arrow, and the calcium stearate (CaSt) monolayer does not show any such phase transition, but monolayer collapse occurs at $\pi_c \approx 70$ and 68 mN/m having $A_c \approx 21.4$ and 20.5 $Å^2$ for Mg^{2+} and Ca^{2+} ions as shown in Figs. 1(a) and 1(b), respectively. Tilted to untilted phase transitions of stearic acid monolayers can also be identified from the finite discontinuity in the isothermal compressibility (κ), where $\kappa = -1/A(\partial A/\partial \pi)_T$ [13]. Variations of κ with π in the presence of Mg^{2+} and Ca^{2+} ions and for two different subphase pH conditions are shown in Figs. 1(f) and 1(g), respectively, which clearly indicates the related phase transition points of the stearic acid monolayer.

In the presence of Zn^{2+} and Cd^{2+} ions, the stearic acid monolayer does not show any tilted to untilted phase transition for both lower and higher subphase pH as shown in Figs. 1(c) and 1(d), respectively. However, the zinc stearate (ZnSt) and cadmium stearate (CdSt) monolayers collapse at $\pi_c \approx 56$ and 55 mN/m (corresponding to $A_c \approx 20.5$ and 18.8 $Å^2$) at lower subphase pH and at $\pi_c \approx 58.6$ and 59 mN/m (corresponding to $A_c \approx 16.6$ and 17.6 $Å^2$) at higher subphase pH, respectively. In the presence of Ba^{2+} ions and at lower subphase pH, the stearic acid monolayer shows a tilted to untilted phase transition at ≈7 mN/m and collapse occurs at $\pi_c \approx 56$ mN/m and $A_c \approx 19.2$ $Å^2$. At higher subphase pH, the isotherm nature of the barium stearate (BaSt) monolayer changes significantly and does not show any tilted to untilted phase transition, and instead of that, pressure starts to rise slowly after $A \approx 20.0$ $Å^2$ and a slow rise of π takes place with lowering the A value up to $A \approx 6.6$ $Å^2$. Variations of κ with π in the presence of Zn^{2+}, Cd^{2+}, and Ba^{2+} ions and for both lower and higher subphase pH are also shown in Figs. 1(h), 1(i), and 1(j), respectively. Lower values of A or A_c as obtained for ZnSt, CdSt, and BaSt monolayers at higher subphase pH in comparison with that of lower pH values clearly indicate the occurrence of 2D to 3D structural transitions or collapse of those monolayers on the water surface at lower surface pressure in comparison with the conventional π_c values as obtained for lower subphase pH conditions.

XRR profiles (open circles) and the corresponding fitted curves (solid lines) obtained from the stearic acid films in the presence of Mg^{2+}, Ca^{2+}, Zn^{2+}, Cd^{2+}, and Ba^{2+} ions deposited at 25 mN/m surface pressure and at two different subphases pH ≈ 6.8 and 9.5 are shown in Figs. 2(a)–2(e), respectively. EDPs obtained from the reflectivity analysis are shown in the insets of the corresponding figures. From the EDPs shown in the insets of Figs. 2(a)–2(e), it is clear that monolayers of stearic acid formed on the water surfaces have been deposited as monolayers in the single upstroke of hydrophilic Si substrates for all chosen divalent ions at lower subphase pH, where metal-containing headgroups are attached to the substrate surface and hydrocarbon tails are toward the air. However, from EDPs it is clear that there is a variation in the out-of-plane structures deposited in the single upstroke of hydrophilic Si substrates at higher subphase pH in the presence of all divalent ions. In the presence of Mg^{2+} and Ca^{2+} ions in the water subphase, a monolayer structure has been deposited, and in the presence of Zn^{2+} and Cd^{2+} ions a trilayer structure has formed on the water surface which has been deposited in the single upstroke of hydrophilic Si substrates. However, from the EDPs it is evidenced that the top layer coverage is relatively less. In the presence of Ba^{2+} ions and at higher subphase pH, a multilayer structure forms on the water surface which has

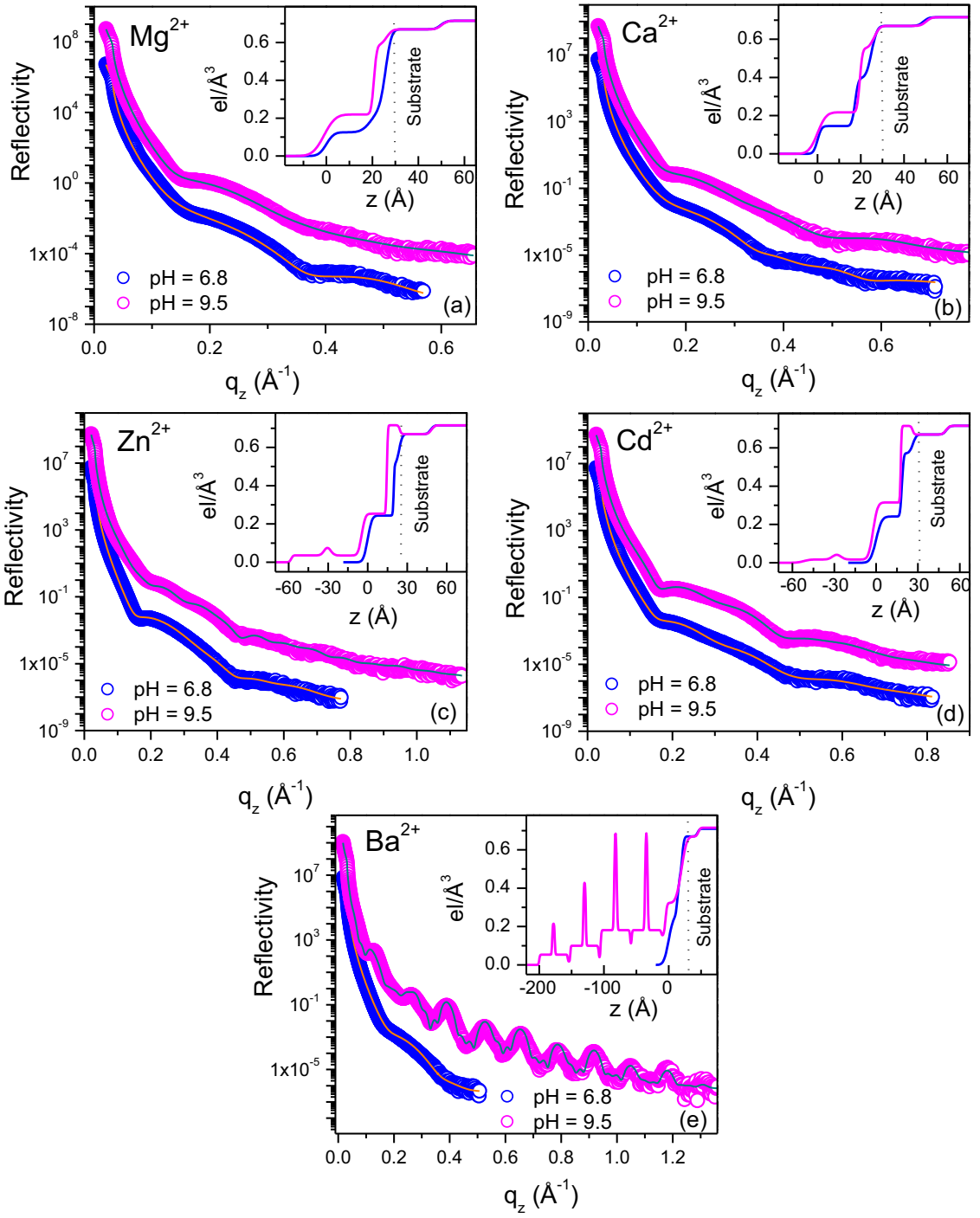

FIG. 2. Observed (open symbols) and calculated (lines) x-ray reflectivity profiles of (a) MgSt, (b) CaSt, (c) ZnSt, (d) CdSt, and (e) BaSt films deposited at 25 mN/m in a single up stroke of Si (001) substrates from lower (≈6.8) and higher (≈9.5) subphase *p*H. Reflectivity profiles and the corresponding fits have been normalized by q_z^4 and also have been shifted vertically for clarity. Insets: EDPs extracted from reflectivity data following monolayer (for MgSt and CaSt), trilayer (for ZnSt and CdSt), and multilayer (for BaSt) models.

been deposited on the hydrophilic Si substrate in the single upstroke. If we consider the electron density of the compact hydrocarbon layer is ≈0.32 electrons/Å^3, then the coverages of the different molecular layers can be obtained. In the presence of Mg^{2+} ions, the monolayer coverages are 41% and 69% at lower and higher subphase *p*H, respectively, whereas for Ca^{2+} ions, the corresponding monolayer coverages are 47% and 69%, respectively. In the presence of Zn^{2+} ions, at lower subphase *p*H, monolayer coverage is 76%, but at higher subphase *p*H, the layer coverages are 79%, 11%, and 11% from substrate to air side, respectively. For Cd^{2+} ions, monolayer coverage at lower *p*H is 76% but at higher *p*H, layer coverages are 98%, 6%, and 6% from substrate to air side, respectively. In the presence of Ba^{2+} ions, monolayer coverage is 68%, whereas at higher subphase *p*H, a multilayer forms and the layer coverage decreases from 99% to 17% from

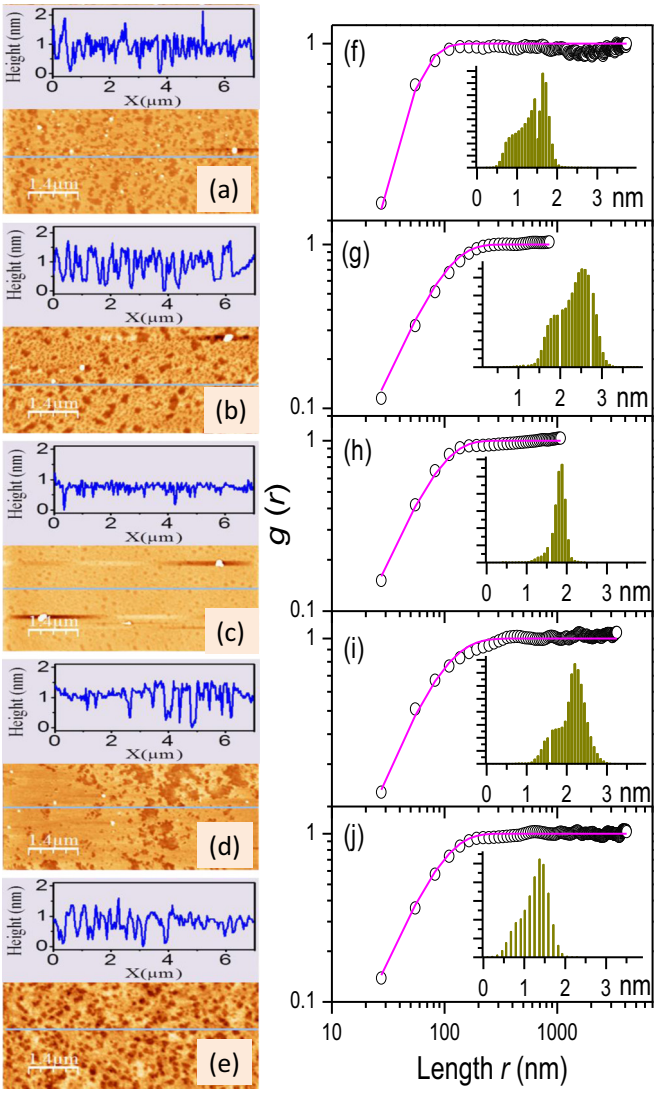

FIG. 3. Left column: AFM images of (a) MgSt, (b) CaSt, (c) ZnSt, (d) CdSt, and (e) BaSt films deposited at 25 mN/m in a single up stroke of Si (001) substrates from lower (≈6.8) subphase pH. Scan area: $7 \times 7\,\mu m^2$. Insets show typical line profiles. Right column: corresponding height-difference correlation obtained from (f) MgSt, (g) CaSt, (h) ZnSt, (i) CdSt, and (j) BaSt films. Insets show typical height histograms.

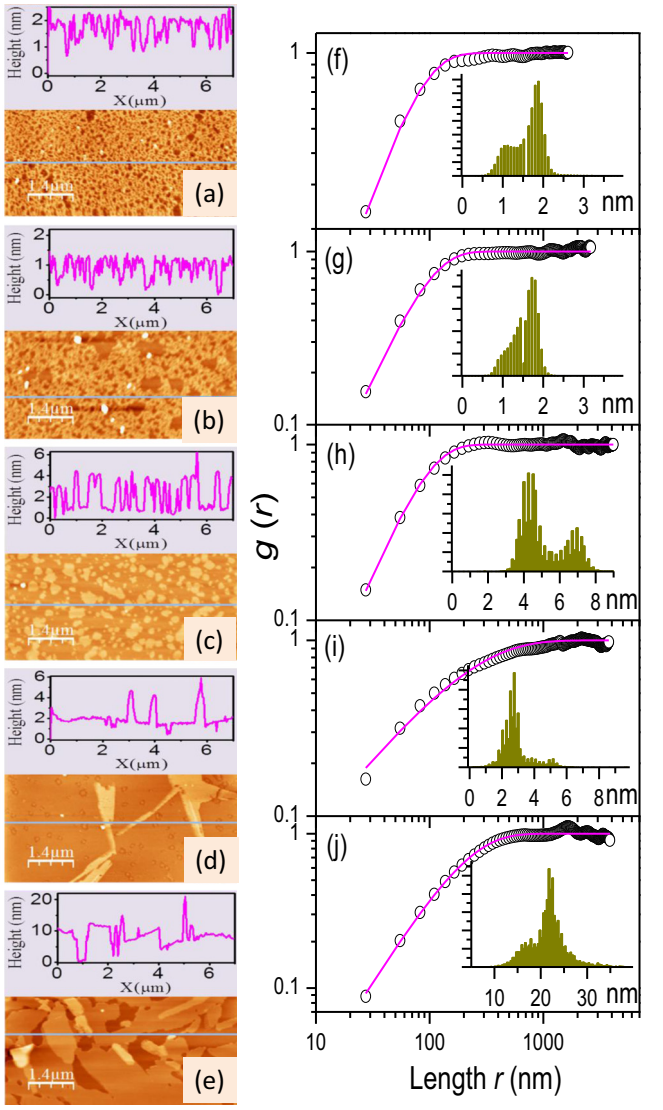

FIG. 4. Left column: AFM images of (a) MgSt, (b) CaSt, (c) ZnSt, (d) CdSt, and (e) BaSt films deposited at 25 mN/m in a single up stroke of Si (001) substrates from higher (≈6.8) subphase pH. Scan area: $7 \times 7\,\mu m^2$. Insets show typical line profiles. Right column: corresponding height-difference correlation obtained from (f) MgSt, (g) CaSt, (h) ZnSt, (i) CdSt, and (j) BaSt films. Insets show typical height histograms.

substrate to air side, respectively. The formation of trilayer and multilayer structures at such lower pressure of 25 mN/m is unusual as at this pressure usually a monolayer exists on the water surface and as a result only monolayer deposits in a single upstroke of hydrophilic Si substrate. Thus, in the presence of a specific divalent ion and at higher subphase pH, a specific headgroup-ion interaction takes place that modifies the elastic behavior of the monolayer and introduces monolayer collapse or structural modulation at lower surface pressure in comparison with the value as obtained from the lower subphase pH condition.

AFM images depicting the surface topography of the MgSt, CaSt, ZnSt, CdSt, and BaSt films deposited at lower pH (≈6.8) are shown in Figs. 3(a)–3(e), respectively, whereas the corresponding height-difference correlation functions obtained from the films are shown in Figs. 3(f)–3(j), respectively. Height distributions of the deposited films are shown in the insets of the corresponding figures. AFM images of the MgSt, CaSt, ZnSt, CdSt, and BaSt films deposited at higher pH (≈9.5) are shown in Figs. 4(a)–4(e), respectively, whereas the corresponding height-difference correlation functions obtained from the deposited films are shown in Figs. 4(f)–4(j), respectively, and the corresponding height distributions are shown in the insets of the corresponding figures. Line profiles obtained from the AFM images are also shown in the insets of corresponding figures to extract the height information of the deposited films. Films deposited at lower pH in the presence of all cations show nearly smooth morphology with the presence of very small pinhole

TABLE I. Films, saturation surface roughness (σ_0), correlation length (ξ), scaling exponent (H), and fractal dimension (D) obtained from the analysis of the AFM images.

Film type	pH	σ_0 (Å)	ξ (Å)	H	D
MgSt		3.6	412	0.74	1.26
CaSt		3.4	933	0.81	1.19
ZnSt	6.8	7.6	818	0.80	1.20
CdSt		3.7	769	0.64	1.36
BaSt		3.2	878	0.80	1.20
MgSt		5.1	708	0.71	1.29
CaSt		3.7	936	0.76	1.24
ZnSt	9.5	12.85	878	0.79	1.21
CdSt		4.1	1946	0.40	1.60
BaSt		39.6	1921	0.60	1.40

type defects and the line profiles indicate the maximum height of ≈20 Å, which is the signature of asymmetric monomolecular layers or simply monolayer heights. Height histograms obtained from the different films also show that the peak values of the distributions, i.e., the film heights, vary between ≈15.0 and 26.0 Å. For self-affine rough surfaces, the out-of-plane fluctuations are expressed by height-difference correlation function $g(r) = 2\sigma_0^2[1 - \exp\{-(r/\xi)^{2H}\}]$, where r is the radial distance between two points, σ_0 is the saturation roughness, ξ is the correlation length, and H is called the roughness or Hurst exponent, which is related with the fractal dimension (D) as $D = d - H$; d is the dimensionality of the system [66,67]. Height-difference correlation functions $g(r)$ are plotted for all the deposited films and the obtained fitting parameters are listed in Table I. For Mg^{2+} and Ca^{2+} ions, films deposited at higher pH also show smooth morphology with very little pinhole type defects and the line profiles show the height of ≈20 Å, which is again the signature of monolayer deposition. Peak values of the height histograms also show that the film heights vary between ≈18.0 and 19.0 Å. However, in the presence of Zn^{2+} and Cd^{2+} ions, films deposited at higher pH show patchlike structures with a maximum height of ≈48 Å determined from the line profiles, which is a signature of bilayer thickness. Thus, in comparison with the x-ray reflectivity results, the lower monolayer thickness is not visible from the line profile. Height histograms obtained from the ZnSt film deposited at higher pH show a bimodal distribution with the peak values at ≈42.4 and 69.2 Å, which is the signature of bilayer and trilayer (total film) thickness, respectively. Height histograms obtained from the CdSt film deposited at higher pH show a weak bimodal distribution with the peak values at ≈26.9 and 52.1 Å, which is the signature of monolayer and bilayer thickness, respectively. Probably due to the presence of a much less covered bilayer on top of the monolayer, total film thickness is not visible in the height histogram. BaSt films deposited at higher subphase pH show totally random domain structures. From the line profile it is clear that a multilayered structure has been deposited having a maximum height of ≈202 Å. Here also the monolayer attached with the substrate surface is not visible from the line profile if the film thickness is compared with the x-ray reflectivity results. However, height histograms obtained from the BaSt film deposited at higher

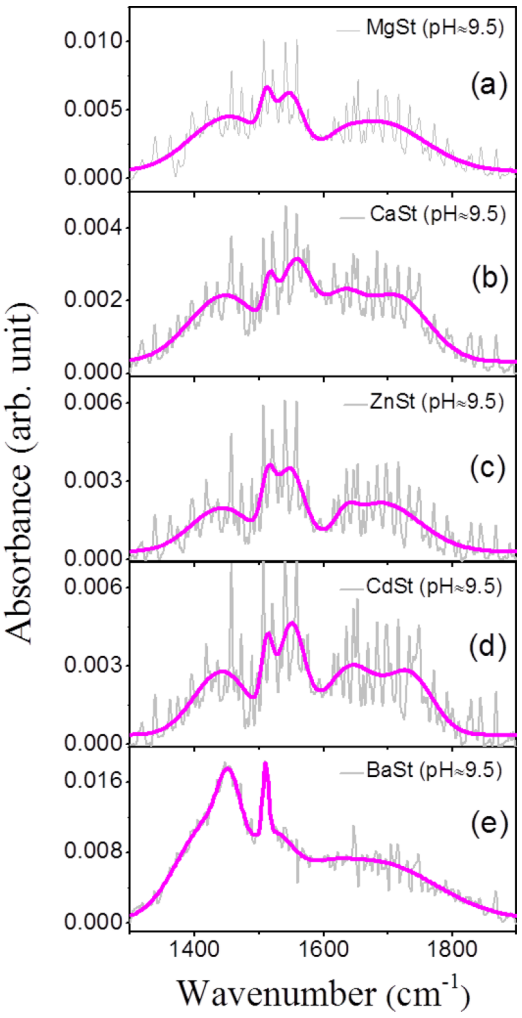

FIG. 5. ATR-FTIR spectra of (a) MgSt, (b) CaSt, (c) ZnSt, (d) CdSt, and (e) BaSt films deposited at 25 mN/m from higher (≈9.5) subphase pH. Colored lines (magenta) are the fitted curves using multiple peaks.

pH show the peak value at ≈221 Å, which is the signature of total film thickness as obtained from the x-ray reflectivity. Height-difference correlation functions $g(r)$ are also plotted for all the films deposited at higher pH and the parameters obtained from the fitting are listed in Table I. From the obtained fitting parameters it is clear that the correlation length (ξ) and the fractal dimension (D) are slightly increased for the films deposited at higher subphase pH. Surface roughness (σ_0) is also increased due to the formation of a less compact layered structure.

FTIR spectra of all the M-St LB films deposited at higher subphase pH are shown in Figs. 5(a)–5(e). FTIR measurements were taken to obtain the information of the specific metal-headgroup coordination from the deposited films. Metal-carboxylate complexes introduce a shift in the positions of the asymmetric (ν_a) and symmetric (ν_s) stretch modes of the COO− group from the free carboxylate ion values. It is known that the carboxylate ion may coordinate to a metal ion in three different ways: unidentate coordination, bidentate chelating coordination, and bidentate bridging coordination

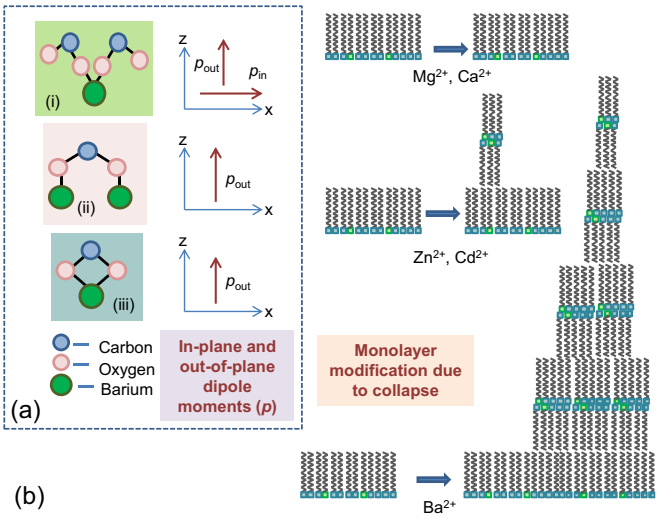

FIG. 6. (a) Cartoon to show the (i) unidentate, (ii) bidentate bridge, and (iii) bidentate chelate coordinated headgroups and the corresponding effective in-plane and out-of-plane dipole moment components. (b) Three different structural modifications of stearic acid Langmuir monolayer at higher (≈9.5) subphase pH and lower surface pressure (25 mN/m), i.e., the formation of monolayer (for MgSt and CaSt), trilayer (for ZnSt and CdSt), and multilayer (for BaSt) structures.

[49,54], which are shown as a cartoon in Fig. 6(a). In the unidentate coordination the gap (Δ) between the ν_s and ν_a is much larger than in the free ion. The opposite trend is observed in the bidentate chelating complex where the Δ is smaller than that of the free ion. In the bidentate bridging complex, however, Δ is nearly the same as observed in free ions but the positions are shifted according to specific metal ions [49,54]. The FTIR spectra shown in Figs. 5(a)–5(e) are fitted by considering multiple peaks and their positions are tabulated in Table II. If the lower peak is assigned for ν_s and another peak is assigned for the scissoring vibration of the methylene group (δ_s), then the other peaks found at higher values are for the ν_a and the highest is for C=O stretching vibrations. For Mg^{2+}, Ca^{2+}, Zn^{2+}, Cd^{2+}, and Ba^{2+} ions, ν_s is observed at 1452, 1447, 1442, 1442, and 1422 cm^{-1}, whereas for each ion ν_a is observed at two different positions. In the presence of Mg^{2+} ions, ν_a are observed at 1548 and 1630 cm^{-1}, which give Δ values of 96 and 178 cm^{-1}, respectively. In the presence of Ca^{2+} ions, ν_a are observed at 1557 and 1625 cm^{-1} and hence the obtained Δ values are 110 and 178 cm^{-1}, respectively. Two ν_a's at 1547 and 1634 cm^{-1} are observed in the presence of Zn^{2+} ions, which give the Δ values of 105 and 192 cm^{-1}, respectively. In the presence of Cd^{2+} ions, ν_a are observed at 1550 and 1641 cm^{-1} and hence two Δ values of 108 and 199 cm^{-1} are obtained. In the presence of Ba^{2+} ions, ν_a are observed at 1510 and 1599 cm^{-1} for which two Δ values of 88 and 177 cm^{-1} are obtained. The available Δ value for the free acetate ion is ≈140 cm^{-1} [68]. Thus, stearic acid in the presence of all ions, i.e., for MgSt, CaSt, ZnSt, CdSt, and BaSt films, metal carboxylates take unidentate coordination as $\Delta_2 > \Delta$ and at the same time the presence of bidentate chelate coordination is also prominent as $\Delta_1 < \Delta$. The peak intensity values at ν_{a1} and ν_{a2}, i.e., for bidentate chelate (C) and unidentate (U) coordination and their ratio (U/C), are also tabulated in Table II. The U/C value is minimum for the Ba^{2+} ion and then for the Zn^{2+}, Cd^{2+}, Mg^{2+}, and Ca^{2+} ions, respectively. Thus, from the U/C values it is clear that the relatively higher values of U/C for the MgSt and CaSt films are possibly related with the monolayer formation, whereas the minimum value of U/C for the BaSt film is possibly related with the formation of the multilayered structure. Intermediate values of U/C for the ZnSt and CdSt films are probably related with the trilayer structure.

From the isotherms it is clear that at lower subphase pH, stearic acid behaves as a monolayer on the water surface in the presence of all divalent ions with the typical known phase transitions and the collapse behaviors. At higher subphase pH, isotherm behaviors modify depending upon the presence of specific divalent ions. In the presence of Mg^{2+} and Ca^{2+} ions at higher pH, stearic acid behaves as a monolayer before the collapse point and generally 2D to 3D structural transformation occurs after the monolayer collapse which has occurred at higher surface pressure ($\pi_c > 60$ mN/m). In the presence of Zn^{2+} and Cd^{2+} ions at higher subphase pH, stearic acid isotherms show nearly similar behaviors; however, for Zn^{2+} ions a greater decrease in the area per molecule is observed in the condensed phase of the monolayer. In the presence of Ba^{2+} ions and at higher subphase pH, a stearic acid isotherm modified as surface pressure starts to rise slowly after $A = 20.0$ Å^2 and finally stops at $\pi = 35.8$ mN/m with $A = 6.6$ Å^2. Thus, such a considerable decrease in the area per molecule for Zn^{2+}, Cd^{2+}, and Ba^{2+} ions clearly indicates the modification of the monolayer structure. The variations in the macroscopic features obtained from the π-A isotherms of stearic acid monolayers are explained using microscopic information obtained from the x-ray scattering, spectroscopic, and microscopic techniques. The small area per molecule as obtained from the isotherms in the presence of Zn^{2+} and Cd^{2+} ions at higher subphase pH is related with the monolayer

TABLE II. Assigned ATR-FTIR peaks of stearic acid LB films in the presence of Mg^{2+}, Ca^{2+}, Zn^{2+}, Cd^{2+}, and Ba^{2+} ions at higher subphase pH (≈9.5).

	ν_s	$\delta(CH_2)$	ν_{a1}	ν_{a2}	$\nu_{C=O}$	Δ_1	Δ_2	$\Delta_{(C=O)}$	U	C	U/C
MgSt	1452	1511	1548	1630	1683	96	178	231	0.0040	0.0061	0.66
CaSt	1447	1516	1557	1625	1710	110	178	263	0.0023	0.0032	0.72
ZnSt	1442	1514	1547	1634	1688	105	192	246	0.0021	0.0035	0.60
CdSt	1442	1513	1550	1641	1734	108	199	292	0.0030	0.0047	0.63
BaSt	1422	1453	1510	1599	1677	88	177	255	0.0071	0.0181	0.39

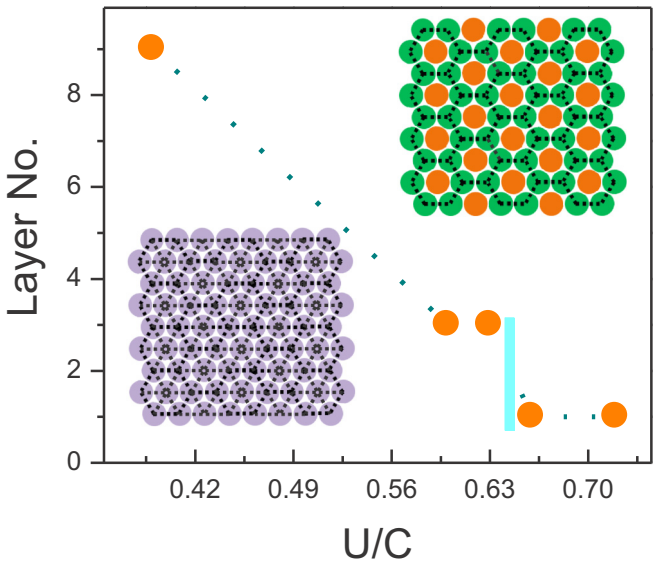

FIG. 7. Out-of-plane layer numbers with the variation of U/C, i.e., the ratio of unidentate and bidentate chelate coordinated headgroups formed in Langmuir monolayer obtained from FTIR peak intensity. Lower inset: probable packing structure of pure monolayer headgroups. Upper inset: probable packing structure of coexisting unidentate and bidentate chelate coordinated headgroups.

to trilayer formation as evidenced from the EDPs obtained from the x-ray reflectivity analysis and supported by the AFM line profiles. Similarly, comparing with the isotherm data obtained from the lower and higher subphase pH conditions, it is clear that the very small area per molecule as obtained from the isotherm in the presence of Ba^{2+} ions at higher subphase pH is related with the monolayer to multilayer formation as evidenced from the x-ray reflectivity and AFM studies. All structural modifications are shown as a cartoon in Fig. 6(b).

Spectroscopic results again give more insight into the bonding information in molecular level to relate the formation of trilayer or multilayer structures with the specific metal-headgroup interactions. From FTIR spectroscopy it is evidenced that at higher subphase pH, both unidentate and bidentate chelate coordinations have formed in the acid headgroups in the presence of all divalent ions. It is known that in bidentate chelate coordination only an out-of-plane dipole moment component exists, whereas for unidentate coordination both in-plane and out-of-plane components are present [55,56]. Due to the presence of a greater amount of unidentate coordination as evidenced from the U/C values for the Mg^{2+} and Ca^{2+} ions, in-plane dipole-dipole interaction is greater, which hinders the multilayer formation with barrier compression and as a result the monolayer structure is maintained. On the other hand, due to the presence of a greater amount of bidentate chelate coordination for Ba^{2+} ions, out-of-plane dipole-dipole interaction is stronger and as a result a multilayer structure easily forms with barrier compression. However, for Zn^{2+} and Cd^{2+} ions, the U/C value is intermediate so the amount of chelate coordination or out-of-plane dipole-dipole interaction is not so high and hence only the trilayer structure coexists with the monolayer with barrier compression. Thus, the relative coverages of two different domains of metal-headgroup coordinations are responsible for such monolayer, trilayer, and multilayer formation. The formation of an ion-dependent layer number with U/C value is plotted in Fig. 7. The hexagonal headgroup structures formed by the pure stearic acid are shown in the lower inset of Fig. 7, whereas the combination of two different metal-headgroup coordinated forms is shown in the upper inset. It is clear from the plot that a critical U/C value of ≈0.66 exists from which the monolayer structure is maintained. The result is very similar to the characteristics of two-dimensional percolated networks. In the percolated system, a giant connectivity exists above a threshold point called critical percolation p_c which is related with the system geometry. In 2D, for hexagonal bond percolation $p_c = 1 - 2\sin(\pi/18) \approx 0.66$ [58–60], which matches the obtained critical value of U/C from which a large in-plane connectivity exists to keep the monolayer structure unaltered. Thus, for U/C ≥ 0.66 the 2D structure formed by the headgroups of unidentate coordination is largely connected by the in-plane dipole moments that help to keep the monolayer structure unaffected. The collapse of biphasic systems is thus regulated by the percolated networks and thus a two-dimensional percolation model can give more insight into the monolayer collapse behaviors.

IV. CONCLUSIONS

We have studied the 2D to 3D structural transformation of stearic acid Langmuir monolayers in the presence of different divalent cations dissolved in the subphase at lower (≈6.8) and higher pH (≈9.5). Deposited films at lower surface pressure (25 mN/m) and lower pH for all cations show the same monolayer structures, which is due to no formation of chelate coordination. However, at higher subphase pH, stearic acid molecules remain as monolayer in the presence of Mg^{2+} and Ca^{2+} ions, but the monolayer transforms into a trilayer structure in the presence of Zn^{2+} and Cd^{2+} ions, and transforms into multilayer in the presence of Ba^{2+} ions, which are confirmed from both XRR and AFM analysis. FTIR spectroscopy data reveal that the relative amounts of bidentate chelate (C) and unidentate (U) coordinations present in the monolayer headgroups are responsible for such 2D to 3D structural transitions. If U/C is higher than the critical value (p_c) of 0.66, the 2D structure formed by the unidentate coordination is largely connected by the in-plane dipole moments that help to keep the monolayer structure unaltered, otherwise a trilayer or multilayer structure forms depending upon the relative amount of the unidentate and bidentate chelate coordinations. The two-dimensional lattice percolation model explains such collapse behaviors of the fatty acid monolayer in the presence of different divalent ions.

ACKNOWLEDGMENT

The authors acknowledge financial support from Department of Science and Technology (DST), Nano Mission, India [Grant No. SR/NM/NS-1035/2013 (G)].

[1] G. L. Gaines, *Insoluble Monolayers at Liquid-Gas Interfaces* (Interscience, New York, 1966).
[2] M. C. Petty, *Langmuir-Blodgett Films: An Introduction* (Cambridge University Press, New York, 1996).
[3] V. M. Kaganer, H. Möhwald, and P. Dutta, Rev. Mod. Phys. **71**, 779 (1999).
[4] V. Krishnan, K. Sakakibara, T. Mori, J. P. Hill, and K. Ariga, Curr. Opin. Colloid Interface Sci. **16**, 459 (2011).
[5] R. M. Leblanc, Curr. Opin. Chem. Biol. **10**, 529 (2006).
[6] A. Baszkin, Adv. Colloid Interface Sci. **128–130**, 111 (2006).
[7] H. Brockman, Curr. Opin. Struct. Biol. **9**, 438 (1999).
[8] T. Hianik, Acta Phys. Slovaca, **56**, 685 (2006).
[9] J. R. Siqueira, Jr., L. Caseli, F. N. Crespilho, V. Zucolotto, and O. N. Oliveira, Jr., Biosens. Bioelectron. **25**, 1255 (2010).
[10] C. Gourier, J. Daillant, A. Braslau, M. Alba, K. Quinn, D. Luzet, C. Blot, D. Chatenay, G. Grübel, J.-F. Legrand, and G. Vignaud, Phys. Rev. Lett. **78**, 3157 (1997).
[11] H. Diamant, T. A. Witten, C. Ege, A. Gopal, and K. Y. C. Lee, Phys. Rev. E **63**, 061602 (2001).
[12] H. Diamant and T. A. Witten, Phys. Rev. E **88**, 012401 (2013).
[13] S. Ställberg-Stenhagen and E. Stenhagen, Nature (London) **156**, 239 (1945).
[14] G. A. Overbeck and D. Mobius, J. Phys. Chem. **97**, 7999 (1993).
[15] T. E. Goto and L. Caseli, Langmuir **29**, 9063 (2013).
[16] H. E. Ries, Jr., Nature (London) **281**, 287 (1979).
[17] H. E. Ries, Jr. and W. A. Kimball, J. Phys. Chem. **59**, 94 (1955).
[18] K. S. Birdi and D. T. Vu, Langmuir **10**, 623 (1994).
[19] D. Vollhardt, T. Kato, and M. Kawano, J. Phys. Chem. **100**, 4141 (1996).
[20] S. Kundu, A. Datta, and S. Hazra, Langmuir **21**, 5894 (2005).
[21] S. Kundu, A. Datta, and S. Hazra, Phys. Rev. E **73**, 051608 (2006).
[22] S. Kundu and D. Langevin, Colloids Surf. A: Physicochem. Eng. Aspects **325**, 81 (2008).
[23] C. Ybert, W. Lu, G. Möller, and C. M. Knobler, J. Phys. Chem. B **106**, 2004 (2002).
[24] M. M. Lipp, K. Y. C. Lee, D. Y. Takamoto, J. A. Zasadzinski, and A. J. Waring, Phys. Rev. Lett. **81**, 1650 (1998).
[25] E. Hatta, H. Hosoi, H. Akiyama, T. Ishil, and K. Mukasa, Eur. Phys. J. B **2**, 347 (1998).
[26] E. Hatta and J. Nagao, Phys. Rev. E **67**, 041604 (2003).
[27] U. K. Basak and A. Datta, Phys. Rev. E **91**, 042405 (2015).
[28] Z. Wang, S. B. Hall, and R. H. Notter, J. Lipid Res. **36**, 1283 (1995).
[29] B. Robertson and H. L. Halliday, Biochim. Biophys. Acta **1408**, 346 (1998).
[30] R. M. Epand and H. J. Vogel, Biochim. Biophys. Acta **1462**, 11 (1999).
[31] L. V. Chernomordik and M. M. Kozlov, Annu. Rev. Biochem. **72**, 175 (2003).
[32] S. S. Vogel and J. Zimmerberg, Proc. Natl. Acad. Sci. USA **89**, 4749 (1992).
[33] R. Vishwanathan, D. K. Schwartz, J. Garnaes, and J. A. N. Zasadzinski, Langmuir **8**, 1603 (1992).
[34] D. K. Schwartz, R. Viswanathan, J. Garnaes, and J. A. Zasadzinski, J. Am. Chem. Soc. **115**, 7374 (1993).
[35] S. Cantin, M-C. Fauré, F. Perrot, and M. Goldmann, J. Phys. Chem. B, **117**, 16275 (2013).
[36] A. Datta, J. Kmetko, A. G. Richter, C. J. Yu, P. Dutta, K. S. Chung, and J. M. Bai, Langmuir **16**, 1239 (2000).
[37] V. M. Kaganer, I. R. Peterson, R. M. Kenn, M. C. Shish, M. Durbin, and P. Dutta, J. Chem. Phys. **102**, 9412 (1995).
[38] S. W. Barton, B. N. Thomas, S. A. Rice, B. Lin, J. B. Peng, J. B. Ketterson, and P. Dutta, J. Chem. Phys. **89**, 2257 (1988).
[39] J. Kmetko, A. Datta, G. Evmenenko, and P. Dutta, J. Phys. Chem. B **105**, 10818 (2001).
[40] A. Datta, J. Kmetko, C. J. Yu, A. G. Richter, K. S. Chung, J. M. Bai, and P. Dutta, J. Phys. Chem. B **104**, 5797 (2000).
[41] V. Dupres, S. Cantin, F. Benhabib, F. Perrot, P. Fontaine, and M. Goldmann, Langmuir **16**, 10189 (2000).
[42] G. Brezesinski, D. Vollhardt, K. Iimura, and H. Cölfen, J. Phys. Chem. C **112**, 15777 (2008).
[43] S. Kundu, Colloids Surf., A **348**, 196 (2009).
[44] M. D. Phan, J. Lee, and K. Shin, J. Oleo Sci. **65**, 385 (2016).
[45] C. Fradin, A. Braslau, D. Luzet, M. Alba, C. Gourier, J. Daillant, G. Grübel, G. Vignaud, J. F. Legrand, J. Lal, J. M. Petit, and F. Rieutord, Phys. B (Amsterdam, Neth.) **248**, 310 (1998).
[46] C. Gourier, C. M. Knobler, J. Daillant, and D. Chatenay, Langmuir **18**, 9434 (2002).
[47] D. Choi, J. H. Moon, H. Kim, B. J. Sung, M. W. Kim, G. Y. Tae, S. K. Satija, B. Akgun, and C.-J. Yu, Soft Matter **8**, 8294 (2012).
[48] E. Le Calvez, D. Blaudez, T. Buffeteau, and B. Desbat, Langmuir **17**, 670 (2001).
[49] K. Y. C. Lee, Annu. Rev. Phys. Chem. **59**, 771 (2008).
[50] D. Vaknin, W. Bu, S. K. Satija, and A. Travesset, Langmuir **23**, 1888 (2007).
[51] W. Bu and D. Vaknin, Langmuir **24**, 441 (2008).
[52] M. Flasiński, M. Gawryś, M. Broniatowski, and P. Wydro, Biochim. Biophys. Acta **1858**, 836 (2016).
[53] K. Das and S. Kundu, Colloids Surf., A **492**, 54 (2016).
[54] K. Nakamoto, *Infrared and Raman Spectra of Inorganic and Coordination Compounds* (Wiley, New York, 1986).
[55] S. Mukherjee and A. Dutta, Phys. Rev. E **83**, 041604 (2011).
[56] S. Mukherjee and A. Datta, Phys. Rev. E **84**, 041601 (2011).
[57] A. Gopal and K. Y. C. Lee, J. Phys. Chem. B **110**, 22079 (2006).
[58] G. R. Grimmett, *Percolation* (Springer-Verlag, New York, 1999).
[59] D. Stauffer and A. Aharony, *Introduction to Percolation Theory* (Taylor & Francis, Washington, DC, 1992).
[60] D. J. Jacobs and M. F. Thorpe, Phys. Rev. E **53**, 3682 (1996).
[61] J. Daillant and A. Gibaud, *X-Ray and Neutron Reflectivity: Principles and Applications* (Springer, Berlin, 1999).
[62] J. K. Basu and M. K. Sanyal, Phys. Rep. **363**, 1 (2002).
[63] M. Tolan, *X-Ray Scattering from Soft Matter Thin Films* (Springer, Berlin, 1999).
[64] L. G. Parratt, Phys. Rev. **95**, 359 (1954).
[65] I. Horcas, R. Fernández, J. M. Gómez-Rodríguez, J. Colchero, J. Gómez-Herrero, and A. M. Baro, Rev. Sci. Instrum. **78**, 013705 (2007).
[66] S. K. Sinha, E. B. Sirota, S. Garoff, and H. B. Stanley, Phys. Rev. B **38**, 2297 (1988).
[67] G. Palasantzas and J. Krim, Phys. Rev. B **48**, 2873 (1993).
[68] S. Kundu, A. Datta, and S. Hazra, Chem. Phys. Lett. **405**, 282 (2005).